Pore constrictions in intervessel pit membranes reduce the risk of embolism spreading in angiosperm xylem

Lucian Kaack[1*], Matthias Weber[2*], Emilie Isasa[3], Zohreh Karimi[4], Shan Li[5], Luciano Pereira[1], Christophe L. Trabi[1], Ya Zhang[6], H. Jochen Schenk[7], Bernhard Schuldt[3], Volker Schmidt[2], Steven Jansen[1]

[1]Institute of Systematic Botany and Ecology, Albert-Einstein-Allee 11, Ulm University, D-89081 Ulm, Germany

[2]Institute of Stochastics, Helmholtzstraße 18, Ulm University, D-89069 Ulm, Germany

[3]Ecophysiology and Vegetation Ecology, Julius-von-Sachs-Institute for Biological Sciences, University of Würzburg, Julius-von-Sachs-Platz 3, D-97082 Würzburg, Germany

[4]Department of Biology, Faculty of Science, Golestan University, Shahid Beheshti St, Gorgan 15759-49138, Iran

[5]Department of Wood Anatomy and Utilization, Research Institute of Wood Industry, Chinese Academy of Forestry, Beijing 100091, China

[6]College of Life Sciences, Anhui Normal University, Beijingdong Road 1, Wuhu 241000, China

[7]Department of Biological Science, California State University Fullerton, Fullerton, CA 92834-6850, USA

Corresponding author: lucian.kaack@uni-ulm.de

* Both authors contributed equally to this study.

SUMMARY

- Embolism spreading in angiosperm xylem occurs via mesoporous pit membranes between vessels. Here, we investigate how the size of pore constrictions in pit membranes is related to pit membrane thickness and embolism resistance.
- In three models, pit membranes are modelled as multiple layers to investigate how pit membrane thickness and the number of intervessel pits per vessel determine pore constriction sizes, the probability of encountering large pores, and air-seeding. These estimations were complemented by measurements of pit membrane thickness, embolism resistance, and number of intervessel pits per vessel (n = 31, 31, and 20 species, respectively).
- Constriction sizes in pores decreased with increasing pit membrane thickness, which agreed with the measured relationship between pit membrane thickness and embolism resistance. The number of pits per vessel affected constriction size and embolism resistance much less than pit membrane thickness. A strong relationship between estimated air-seeding pressures and measured embolism resistance was observed.
- Pore constrictions provide a mechanistic explanation why pit membrane thickness determines embolism resistance, and suggest that hydraulic safety can be uncoupled from hydraulic efficiency. Although embolism spreading remains puzzling and encompasses more than pore constriction sizes, angiosperms are unlikely to have leaky pit membranes, which enables tensile transport of water.

Keywords: air-seeding, angiosperm xylem, embolism, pit membrane, pore constriction, porous medium, vessel, ultrastructural modelling

INTRODUCTION

Xylem sap in vessel-bearing angiosperms crosses numerous intervessel walls from the root to the leaf xylem, depending on the plant size, vessel length, and intervessel connectivity. An average angiosperm vessel is estimated to have about 34,000 intervessel pits, with values for different species varying more than 200-fold, from ca. 500 pits to > 100,000 (sample size, n = 72 species; Fig. S1). Each bordered pit pair has a pit membrane, which is mainly composed of ca. 20 nm wide cellulose microfibril aggregates. These pit membranes develop from the primary cell wall and middle lamella, and have a mean diameter of 4.8 ± 2.4 µm (n = 43 species; Jansen et al., 2009, 2011). Before pit membranes become hydraulically functional, hemicellulose and pectin compounds are enzymatically removed (O'Brien, 1970; Herbette *et al.*, 2015; Klepsch *et al.*, 2016). Therefore, fully mature pit membranes are non-woven, fibrous porous media of mainly cellulose, with a thickness between ca. 160 and 1,000 nm (Esau 1977; Pesacreta *et al.*, 2005; Kaack *et al.*, 2019).

Intervessel pit membranes play an important role in plant water transport by providing ca. 50% of the total hydraulic xylem resistance (Choat *et al.*, 2008). They control the immediate entry of gas from neighbouring, embolised conduits, and may become sites of further embolism propagation under persistent drought (Zimmermann, 1983; Brodersen *et al.*, 2013; Choat *et al.*, 2016; Brodribb *et al.*, 2016; Roth-Nebelsick, 2019). The lack of a mechanistic understanding of gas bubble movement through pit membranes, which is described as "air-seeding", represents one of the major knowledge gaps in our understanding of water transport in plants (Jansen *et al.*, 2018). It is known that propagation of drought-induced embolism from one vessel to a neighbouring vessel is affected by pore dimensions of intervessel pit membranes, but how pit membrane thickness (T_{PM}; see Table 2 for an overview of the acronyms used) affects pore dimensions and embolism spreading is unclear.

Instead of perfectly flat, two-dimensional structures, as often portrayed in textbooks, pit membranes are porous media with pores that include multiple constrictions, with the respective narrowest constriction in each pore governing flow of water and gas (Fig. 1; Kaack *et al.*, 2019) and, consequently, embolism spreading. Estimates of bottleneck diameters, *i.e.* constriction sizes, vary from 5 nm to well above 200 nm (Fig. 1; Choat *et al.*, 2003; Sano, 2005; Jansen *et al.*, 2009; Hillabrand *et al.*, 2016). Part of this variation is caused by sample preparation for imaging by

scanning electron microscopy (SEM), which induces up to 50% shrinkage of T_{PM} during drying, with frequently enlarged pores and cracks (Shane *et al.*, 2000; Jansen *et al.*, 2008; Zhang *et al.*, 2017). Moreover, the challenge is to quantify size and shape of pit membrane pores in a three-dimensional approach. A three-dimensional model based on transmission electron microscopy (TEM) of fresh and shrunken pit membranes indicated a high porosity (*i.e.* void volume fraction) of 81%, highly interconnected pore systems with non-tortuous, unbending passageways, a lack of dead-end pores, and the occurrence of multiple pore constrictions within a single pore (Zhang *et al.*, 2020). Based on a shrinkage model and gold perfusion experiments, we found that constriction sizes in pit membrane pores vary from 5 to < 50 nm, with an average diameter around 20 nm (Choat *et al.*, 2003, 2004; Zhang *et al.*, 2020). Moreover, the structural characteristics of pit membranes appear to be fairly constant for angiosperm species, despite considerable variation in T_{PM}. Indeed, pore constriction sizes around 20 nm occur both in species with thin (ca. 200 nm) and thick (> 500 nm) pit membranes (Fig. S2), and there is no evidence for large (> 50 nm) pore size differences among species (Zhang *et al.*, 2020). So why then is xylem embolism resistance, which is frequently quantified as the xylem water potential corresponding to 50% loss of the maximum hydraulic conductivity (P_{50}, MPa), so variable within angiosperms (Choat *et al.*, 2012)?

Angiosperm species with thick pit membranes were found to be more resistant to drought-induced embolism than species with thin pit membranes (Jansen *et al.*, 2009; Li *et al.*, 2016). This functional link between T_{PM} and P_{50} is valid at the interspecific and intraspecific level (Lens *et al.*, 2011; Plavcová & Hacke, 2012; Scholz *et al.*, 2013; Schuldt *et al.*, 2016). Variation in T_{PM} is mainly determined by the number of microfibril layers (N_L), with thin pit membranes consisting of fewer microfibril layers than thick pit membranes. Note that N_L can be estimated by assuming that cellulose fibres have a diameter of about 20 nm (Pesacreta *et al.*, 2005), and 20 nm pore spaces between each layer based on gold perfusion experiments (Table 1; Zhang *et al.*, 2020). As such, pit membranes with a thickness between 140 and 1,180 nm (Jansen *et al.*, 2009; Li *et al.*, 2016) include between 4 and 30 layers. In our models, bottlenecks in a given pore are formed by the pore constrictions between cellulose fibres within a single layer. Therefore, the number of constrictions within a pore (N_C) equals N_L (Table 1). Since it is unknown why thin pit membranes are more vulnerable to embolism than thick pit membranes (Jansen *et al.*, 2018), we explore the hypothesis that the likelihood of leaky pores is affected by N_L, which would explain why T_{PM} is related to P_{50}.

The mismatch between pore size estimations based on colloidal gold perfusion, and those calculated from vulnerability curves or air-seeding measurements, resulted in the hypothesis that a very small percentage of pit membranes might contain large, leaky pores (Choat *et al.*, 2003, 2004). These rare pit membrane pores are assumed to account for low air-seeding pressures (< 1 MPa). The idea of such leaky, rare pits was further enhanced when variation in P_{50} at an interspecific level was found to decrease with increasing pit membrane surface area in intervessel walls (Wheeler *et al.*, 2005). The "pit area hypothesis" (Sperry *et al.*, 2006), which was later termed "rare pit hypothesis", provided a possible explanation for low air-seeding pressures, and relied on a largely two-dimensional interpretation of pit membranes (Hacke *et al.*, 2007; Christman *et al.*, 2009, 2012; Plavcová *et al.*, 2013). While the rare pit hypothesis follows a plausible concept that seems well supported by indirect evidence, it cannot be tested because the existence of a rare pit with a leaky pore cannot be observed directly, and is impossible to be verified from a statistical point of view. However, a three-dimensional modelling approach to estimate the likelihood of leaky pits is clearly lacking.

The number of layers in a pit membrane affects the size of the narrowest constriction within a pore that crosses the entire intervessel pit membrane (Fig. 1). Because the pressure difference required for air-seeding is determined by the radius of a meniscus in a pore, the most important dimension of a pore is its minimum diameter, i.e., the diameter of the narrowest bottleneck along the pore. We can think of this diameter as the "effective diameter" of the pore. The entry of an air-water meniscus or a bubble in a pit membrane is determined by the pore with the largest effective diameter within the pit membrane. Thus, air-seeding pressure and the minimum hydraulic resistance at the intervessel level is governed by the pore with the largest effective diameter in all pit membranes of a single vessel.

First, we hypothesise that the effective diameter of each pore becomes smaller with increasing T_{PM} and N_L (Hypothesis 1). This hypothesis is investigated at the individual pit membrane level based on a stochastic pit membrane model. Second, we hypothesise that model-based values of air-seeding pressure largely agree to embolism resistance measurements for a large number of species (Hypothesis 2). Third, we expect that the probability of having a leaky pit membrane is low at the whole vessel level, and affected by both T_{PM} (Li *et al.*, 2016), and the total number of intervessel pits per vessel (N_{PIT}; Hypothesis 3) (Wheeler *et al.*, 2005). The second hypothesis is tested based on experimental data on embolism resistance, and anatomical

measurements, while two further stochastic pit membrane models are developed to test the third hypothesis. Verifying these hypotheses should help us to better understand the functional link between embolism resistance and pit membrane ultrastructure.

MATERIALS AND METHODS

Pit membrane modelling

To better understand the relationship between T_{PM} and P_{50}, we developed three pit membrane models with different levels of complexity. For reasons of simplicity, we assumed the existence of more or less cylindrical pores, which govern transport phenomena. However, we modelled each pore as a three-dimensional object instead of a circular, flat opening (Sperry and Hacke, 2004; Mrad *et al.*, 2018). Following the multi-layered pit membrane model of Zhang *et al.* (2020), we assumed that each pore penetrates a fixed number of microfibril layers. Each of these layers induces a pore constriction of some random radius (Fig. 1e). An important property of each pore is its effective radius, i.e., the radius of the narrowest pore constriction within the entire pore (R_{MIN}, nm). We were especially interested in how R_{MIN} was affected by T_{PM} (Hypothesis 1), how modelled air-seeding pressure based on pore constriction size related to measured embolism resistance (Hypothesis 2), and to what extent the likelihood of leaky pit membranes at the entire vessel level was affected by T_{PM} and/or N_{PIT} (Hypothesis 3).

Selected T_{PM} values spanned a range of 160 to 1,200 nm based on TEM (Jansen *et al.*, 2009; Li *et al.*, 2016). We assumed that the number of pore constrictions (N_C) was equal to the number of microfibril layers N_L, where $N_L = [(T_{PM} + 20) / 40]$, and that the thickness of each layer corresponded to a single microfibril's average diameter of 20 nm (Jansen *et al.*, 2009; Pesacreta *et al.*, 2005), with a distance of 20 nm between neighbouring layers. The latter seemed reasonable based on gold perfusion experiments (Choat *et al.*, 2003, 2004; Zhang *et al.*, 2017, 2020) and the fact that cellulose microfibrils are slightly negatively charged.

We developed three different models to investigate the relationship between T_{PM} and the probability of encountering at least one pore with R_{MIN} larger than a given threshold. While Model 1 was used to estimate pit membrane leakiness at the structural level of a single pit membrane, Models 2 and 3 considered leakiness at the vessel level.

Model 1. Pore constrictions in single intervessel pit membranes

In this model (Fig. 2a), we assumed that a pit membrane comprised a fixed number of pores (N_P), which were independent of each other, but we did not consider the location of pores within a pit membrane. Each pore was defined by a fixed number of pore constrictions (N_C), given by the number of layers N_L. The random radius of each pore constriction was modelled by a left-truncated normal distribution with parameters R_L, μ_R and σ_R, where μ_R and σ_R were mean and standard deviation of the untruncated normal distribution, and R_L was the lower bound for truncation. For a circular pit membrane with a diameter of 5 µm (estimated from n = 43 species, Jansen *et al.* 2009, 2011) and two different scenarios R_L = 2.5 nm, μ_R = 10 nm, σ_R = 7.5 nm (Scenario 1), and R_L = 2.5 nm, μ_R = 50 nm, σ_R = 40 nm (Scenario 2), we estimated an upper bound for the number of pores that might possibly fit into the membrane. The full specifications of the two scenarios were calculated as N_P = 12,000 (Scenario 1), and N_P = 1,100 (Scenario 2). While Scenario 1 was considered to be realistic based on gold perfusion experiments (Zhang *et al.*, 2020), Scenario 2 was taken as a conservative approach. For each pore, we considered N_C-values between 4 and 32, and T_{PM}-values between 140 and 1260 nm (Table 1). The random diameters of pore constrictions of a whole pit membrane was simulated ten times for the Scenarios 1 and 2, with R_{MIN} determined for each pore. Then, for each value of N_C we calculated the percentage of pores with R_{MIN} above a given threshold t, i.e., the percentage of leakiness for the modelled pit membrane. This threshold was chosen at $t = \mu_R + \sigma_R$, i.e., at 35 nm (Scenario 1) and 180 nm (Scenario 2). Furthermore, for each value of N_L, the mean (R_{MIN_mean}) and maximum values (R_{MIN_max}) of the effective radii R_{MIN} obtained in the repeated simulation runs, were calculated.

To compare the results obtained from Model 1 with experimental data on embolism resistance, the theoretical air-seeding pressure was calculated based on R_{MIN_max} and R_{MIN_mean}. For this, a modified Young-Laplace equation was applied:

$$\Delta P = \kappa\, 2\, \gamma \cos(\alpha) / R_{MIN},$$

where ΔP was the pressure required to induce air-seeding, κ was a dimensionless pore shape correction factor which was assumed to be equal to 0.5 (Schenk *et al.* 2015), γ was the surface tension of xylem sap, α represented the contact angle of the gas-xylem sap interface with the solid cellulose microfibril and was assumed to be equal to zero, and R_{MIN} was the narrowest pore constriction radius. We assumed that γ was either 72 or 25 mN/m, which corresponded to the surface tension of pure water and was close to the bulk surface tension of xylem sap (Christensen-

Dalsgaard and Tyree, 2014), and the equilibrium surface tension of xylem sap lipids based on dynamic surface tension (Schenk *et al.*, 2017; Yang *et al.*, 2020).

Models 2 and 3. Leaky pit membranes at the vessel level

Model 2 investigated the occurrence of leaky pit membranes at the vessel level. We first calculated an upper bound for the probability that a leaky pore would run through an entire intervessel pit membrane (Fig. 2b). The minimum requirement needed for a leaky pore was that there existed at least one hole with a radius larger than a given threshold t in each layer. The term hole was used as a substitute for constriction as its diameter might even exceed the length of the pore. We did not account for proper alignment of the holes in Model 2. The probability that at least one large hole existed in each layer, was an upper bound for the probability of encountering at least one pore through the whole membrane with an effective radius larger than t. We assumed that the probability P of encountering a large hole in any given layer is independent of the occurrence of this event in other layers, and constant across all layers. In particular, we assumed that a probability of P = 0.25 represents a safe scenario, whereas P = 0.50 represents a risky scenario. The probability of encountering at least one leaky pore through the whole membrane was given by P^{N_L}. At the entire vessel level, an upper bound for the probability of having a leaky pit membrane (P_{LP}) was given by

$$P_{LP} = 1 - (1 - P^{N_L})^{N_{PIT}}.$$

We estimated N_{PIT} based on the total pit membrane surface area per vessel (A_P) of 72 species using original data and literature data (Fig. S1; Wheeler *et al.*, 2005; Jansen *et al.*, 2011; Lens *et al.*, 2011; Nardini *et al.*, 2012; Scholz *et al.*, 2013; Klepsch *et al.*, 2016). Values of N_{PIT} were not normally distributed (Shapiro-Wilk test, W = 0.84, $p < 0.0001$, n = 65, excluding outliers), and were varying asymmetrically from 510 to 370,755, with a median of 14,188 (IQR: 31,618, Q_1: 4,651 N_{PIT}, Q_3: 36,269, n = 72 species). Since only six species showed N_{PIT}-values above 83,068 (Q_3 + 1.5 * IQR), we took N_{PIT} = 80,000 as a representative maximum value in our graphs, although we investigated the occurrence of leaky pits up to N_{PIT} of 400,000.

Since we did not consider in Model 2 the alignment of holes within successive layers, we effectively assumed that gas could spread between layers of the membrane and then entered through the next large holes of the following layer. Although it is currently unknown whether such an alignment of holes would be required for air-seeding, we incorporated the location of holes in

pit membrane layers in Model 3. More precisely, we modelled pit membranes as a stack of N_L circular layers of cellulose material, with diameter D_P (= 5 µm), and no gap between two adjacent layers. Each layer was perforated by randomly located holes. Since we were interested in pores with a minimum radius larger than a given threshold *t*, holes smaller than this threshold were ignored. Thus, in each layer, we randomly placed a fixed number of large, non-overlapping holes (N_{HOLES}). For simplicity, we chose the threshold *t* as radius for all these holes. Then, we determined the pores that crossed the whole pit membrane. A pore did only traverse all layers if there existed a sequence of holes such that for each pair of adjacent layers, the holes were properly aligned and overlapping (Fig. 2c). Holes without minimal overlapping with holes in adjacent layers were assumed to form dead-ends and ignored. The locations of holes within and across layers were simulated stepwise and repeated 10^6 times for pit membranes with N_L-values between 4 and 12 (Table 1). Details of the implementation are given in the Supporting Information (Method S1). For simplicity, we ignored incomplete overlap of adjacent holes, which could lead to a reduced minimum radius of the resulting pore. Using this model, we modelled a large number of membranes for *t* (hole threshold radius) = 200 nm, D_P = 5 µm, N_L = 4 to 12, and N_{HOLES} = 5 or 10. These values of R_{MIN} and N_{HOLES} were selected to make pit membranes leakier than available evidence suggests, to increase the likelihood of overlapping holes, and to avoid underestimating leakiness. For each scenario, we estimated the probability that at least one leaky pore with $R_{MIN} \geq$ 200 nm crossed an entire pit membrane. Finally, we estimated the probability of leaky pit membranes with at least one large pore for a vessel with 30,000 intervessel pits (N_{PIT}), which was well above the median N_{PIT} of 14,188 intervessel pits (Fig. S1).

Experimental work

The three models were complemented by experimental data on embolism resistance (n = 31 species), T_{PM} measurements at the centre (T_{PM_centre}) and near the edges (T_{PM_edge}) (n = 31 species), and the total intervessel pit membrane area per average vessel (A_P, n = 20 species). The methods applied to obtain these data include well-established, previously published protocols (Wheeler *et al.*, 2005; Sperry *et al.*, 2006; Schuldt et al. 2016; Zhang *et al.* 2020; Kotowska *et al.*, 2020), and are described in detail in the Supporting Information (Method S2). All data include original measurements, except for data retrieved from literature for embolism resistance of five species, and for A_p values of four species.

Statistics and data processing

Data processing, simulations and statistical analyses were performed using Excel, R, and Matlab. Shapiro-Wilk Tests were applied to test for normal distribution. Pearson's Correlation Coefficient were used to test for linear correlation. Basic linear and non-linear regressions were fitted to test whether P_{12}, P_{50}, P_{88}, and the slope of vulnerability curves (S) are related to T_{PM} or A_P, and could be estimated. Only significant regressions with the highest R^2 were considered. For each of the 31 species studied, we estimated air-seeding pressures by integrating their modelled R_{MIN_mean} and R_{MIN_max}, based on T_{PM}, into the equations of the relation between T_{PM} and air-seeding pressure of Model 1. This approach allowed us to compare estimated air-seeding with experimental values of P_{12} and P_{50}. Model 3 was simulated using R (Method S1).

RESULTS

How likely are large pores in a pit membrane for a wide range of pit membrane thicknesses?

Average values of R_{MIN} (R_{MIN_mean}) are very low in Scenario 1 of Model 1, with values below 9 nm for pit membranes with 150 to 1,150 nm in thicknesses (Fig. 3a). The size of R_{MIN} declines considerably with increasing T_{PM}, and the largest ones (R_{MIN_max}) decrease from ca. 40.7 ± 2.7 to 12 ± 1.1nm (Fig. 3a). R_{MIN_max}-values are at least 2.4 times and up to 4.9 times larger than the R_{MIN_mean}-values, decreasing with T_{PM} (Fig. 3a). The likelihood of having an effective diameter ≥ 35 nm approaches zero (0.00005 ± 0.00009, Fig. 3b) when T_{PM} is > 220 nm, or $N_L \geq 6$, thus only occurs in 0.2 out of 12,000 pores.

For Scenario 2 of Model 1, a similar decline of R_{MIN} with increasing T_{PM} is found (Fig. S3), but with steeper declining likelihood values for large pores with T_{PM}. For a T_{PM} of 220 nm the likelihood of containing a large pore (defined in Scenario 2 of Model 1 as ≥ 180 nm in diameter) is nearly zero.

How does pit membrane thickness relate to measured embolism resistance?

The values of T_{PM_mean} vary from 165 nm (± 18 SD) for *Tilia platyphyllos* to 610 nm (± 79 SD) for *Olea europaea*, and the median of T_{PM} is equal to 270 nm (n = 31 species studied; Table S1). The value of T_{PM_centre} is always larger than the value of T_{PM_edge}, with an average difference

of 105 nm, varying from 2.1 nm (*Tilia platyphyllos*) to 297 nm (*Olea europaea*), and increasing with T_{PM}.

P_{50}-values are strongly related to the values of T_{PM_centre} (Table 3; Fig. 4c), with a logarithmic regression showing an R^2-value of 0.57 ($F(2, 29) = 32.0$, $p < 0.001$). An outlier in the T_{PM} vs. P_{50} relationship includes *Corylus avellana*, which shows considerably high T_{PM}-values of ca. 400 nm for a P_{50}–value of -2.02 MPa. Slightly lower correlations are found between the T_{PM_centre} and P_{12} ($F(2, 29) = 24.4$, $p < 0.001$, $R^2 = 0.457$), and between T_{PM_centre} and P_{88} ($F(2, 29) = 34.2$, $p < 0.001$, $R^2 = 0.541$; Table 3). Thus, the T_{PM_centre}-values show a stronger relationship to embolism resistance than T_{PM_mean} and T_{PM_edge}. The average intervessel pit membrane surface area per vessel (A_P, Table S1) shows much lower correlations to P_{50}, P_{12} and P_{88} than all T_{PM} traits, with the strongest correlation between A_p and P_{12} ($F(2, 18) = 7.75$, $p < 0.05$, $R^2 = 0.301$; Table 3).

T_{PM_mean} shows a linear relationship with T_{PM_mean} SD, with larger variation in thick than in thin pit membranes (Pearson's Correlation Coefficient, $r(29) = 0.759$, $p < 0.00001$). Furthermore, we find a power regression with an R^2–value of 0.477 between the slope of vulnerability curves (S) and T_{PM_mean} ($F(2, 29) = 88.4$, $p < .001$, $R^2 = 0.477$; Table 3), with decreasing S being associated with increasing T_{PM_mean}. There is a weaker relation between S and T_{PM_edge}, and a slightly stronger relation to T_{PM_centre} than T_{PM_mean} (Table 3).

Does modelled air-seeding correspond to measured embolism resistance for a wide range of pit membrane thicknesses?

There are clear differences in the estimated air-seeding pressures, depending on the surface tension, and whether the maximum or mean R_{MIN}-values are considered (Fig. 4). For a surface tension of 72 mN/m, estimated air-seeding pressures, which theoretically correspond to P_{12}, are much higher than the P_{12} values measured, and even higher than P_{50} measurements. Regression lines of the T_{PM}-P_{50} and T_{PM}-P_{12} relationship, however, fall well within the estimated air-seeding pressures when a surface tension of 25 mN/m (green lines in Fig. 4a) is considered. Although absolute values of modelled and measured air-seeding (P_{12}) and embolism resistance pressures (P_{50}) do not match (Fig. 4a, 5), they are significantly related to each other (Pearson's Correlation Coefficient, P_{12} to R_{MIN_mean} and R_{MIN_max}: $r(29) = 0.67$ and $r(29) = 0.636$, $p << 0.01$; P_{50} to R_{MIN_mean} and R_{MIN_max}: $r(29) = 0.739$ and $r(29) = 0.732$, $p < 0.00001$; Table 3, Fig. 5). When R_{MIN_max} is considered, estimated air-seeding pressures show a small range, with about 1.2 MPa

for a T_{PM} of 140 nm and up to 2.7 MPa for a T_{PM} of 758 nm (Fig. 5b), which underestimates embolism resistance (Fig. 4a, 5a, 5b). Much higher air-seeding pressures between 5.6 and 10 MPa are obtained for estimations based on R_{MIN_mean}, overestimating embolism resistance (Fig. 4a, 5c, d). There is a clear upper limit of air-seeding pressure for R_{MIN_mean} around ca. 10 MPa, which is achieved for pit membranes with thicknesses $\geq$ 600 nm.

Modelled air-seeding pressures based on R_{MIN_max} are similar but typically lower than the experimental values (Fig. 5a, b). Estimated air-seeding pressures based on R_{MIN_max} are especially close to measured embolism resistance for various species with not very negative P_{12}- and P_{50}-values (Fig. 5a, b), while estimated air-seeding pressures based on R_{MIN_mean} are much higher than P_{12} and P_{50} measurements (Fig. 5c, d).

How likely are leaky intervessel pit membranes at the vessel level?

Based on Model 2, the probability of having a leaky pit membrane in a vessel decreases exponentially with increasing T_{PM} (Fig. 6, Fig. S4). For a fixed T_{PM}, the slope of the relationship between N_{PIT} and the probability of a leaky pore strongly depends on T_{PM} (Fig. S5): steep, exponential slopes are found for thin pit membranes, while low, more linear slopes are found for thick pit membranes. Therefore, T_{PM_mean} and N_{PIT} affect the likelihood of large effective pore radii differently, with N_{PIT} having an unequal effect on the likelihood of having leaky pit membranes.

For the 0.5 likelihood assumption (Fig. S4, S5b), vessels with 820 nm thick pit membranes reach a likelihood of having a leaky pit membrane below 0.20, even in vessels with 400,000 intervessel pits, which means that not even every fifth vessel would have a leaky pit.

For the 0.25 likelihood of Model 2 (Fig. 6, S5a), an exponential change is found for T_{PM_mean}-values between 200 and 300 nm, while little or no effect is seen for T_{PM_mean}-values below 200 nm and above 350 nm. The high and low probability plateaus in the three-dimensional graphs of Model 2 (Fig. 6, S4) suggest the existence of a thin and a thick T_{PM}-range that typically results in leaky or very safe, non-leaky vessels, respectively, independent of N_{PIT}. At the exponential phase of the three-dimensional graph in Fig. 6, an increase in N_{PIT} from 3,000 to 70,000 (i.e. a 23-fold increase) is equivalent to adding about five additional microfibril layers to a pit membrane (i.e. an increase in T_{PM} of 180 nm). Critical T_{PM}-values are higher for the 0.5 likelihood of Model 2 (Fig. S5b, S4), with the largest effect of N_{PIT} for pit membranes between 500 and 700 nm.

The results obtained from Model 3 show that the modelled probability of leaky pit membranes in a vessel with 30,000 intervessel pits (N_{PIT}) decreases exponentially from 0.045 for 140 nm thick pit membranes to < 0.01 for T_{PM}-values above 180 nm (Fig. 7). Assuming 5 or 10 holes per microfibril layer (N_{HOLES}), less than one out of 30,000 pits has a large pore for T_{PM}-values above 220 nm and 340 nm, respectively. Therefore, 220 nm thick pit membranes with a N_{HOLES}-value of 5 have a similar safety as 340 nm thick pit membranes with an N_{HOLES}-value of 10.

DISCUSSION

The results described above indicate that the chance of having large pores in pit membranes decreases strongly with the number of constrictions, and therefore T_{PM} (Hypothesis 1). This finding is independent of the actual size of pore constrictions, and supported by a strong relation between embolism resistance and T_{PM} (Jansen *et al.*, 2009, 2018; Lens *et al.*, 2011; Scholz *et al.*, 2013; Schuldt *et al.*, 2016; Li *et al.*, 2016). Modelled air-seeding values are significantly related to measured embolism resistance (Hypothesis 2), although they differ in absolute values. There is a good agreement when the dynamic surface tension of xylem sap is taken into account (Yang *et al.*, 2020), but embolism spreading does not seem to represent a function of pore constriction size (R_{MIN_max} and R_{MIN_mean}) only. Our results also suggest that the likelihood of having a leaky pit membrane within a vessel is extremely low (Hypothesis 3), and mainly determined by T_{PM}. Overall, pore constrictions provide a mechanistic explanation why embolism resistance is correlated with T_{PM}, and why pit membranes provide hydraulic safety to angiosperm xylem.

The most narrow pore constriction becomes strongly reduced in size with increasing pit membrane thickness

The three models developed show a negative correlation between the simulated pore sizes and T_{PM}, which is reflected in a low probability of large pores, both at the level of an individual pit membrane and an entire vessel. Based on Model 1, the chance of having a large pore in a pit membrane thicker than 180 nm is close to zero. Interestingly, the thinnest pit membranes measured in this study (ca. 165 to 180 nm) are likely to represent a lower limit for T_{PM}, since earlier records of T_{PM} below 150 nm (Jansen *et al.*, 2009; Li *et al.*, 2016) are likely artefacts due to shrinkage (Zhang *et al.*, 2017, 2018, 2020; Kotowska *et al.*, 2020). Thus, angiosperm pit membranes seem to have at least four or five layers of cellulose microfibrils and pore constrictions, which keeps the

number of large pores very low for most species. There is a clear conceptual relationship between the thickness of a fibrous porous medium, and the size of the narrowest pore constriction as also seen for non-woven, fibrous geotextiles that differ in thickness (Aydilek *et al.*, 2007).

Model 2 suggests that the probability of encountering large pores in intervessel walls follows an exponential pattern over a fairly narrow range of T_{PM}, with critical T_{PM}-values between 200 to 300 nm and 500 to 700 nm for a 0.25- and 0.50-likelihood, respectively, of having at least one hole larger than t within a single microfibril layer. Although this likelihood cannot be accurately determined due to our limited understanding of air-seeding, we believe that a realistic likelihood would probably lay around 0.25, with 0.50 being too conservative. This assumption is supported by the steeper increase in embolism resistance within the lower T_{PM}-range between 140 to 340 nm than in the higher T_{PM}-range, and by the probabilities of large pores in pit membranes approaching zero for $T_{PM} > 250$ nm in Model 1 and 3. We applied a logarithmic regression between P_{50}, P_{12} and T_{PM} (Fig. 4b, 4c), unlike a linear scaling that was previously suggested (Lens *et al.*, 2011; Li *et al.*, 2016). Interestingly, this logarithmic regression has P_{50} –values approaching 10 MPa for a T_{PM} of > 1,000 nm (Fig. 4a), which corresponds to the upper physical limit of both xylem water potential and the maximum T_{PM}–value measured (Vilagrosa *et al.*, 2003; Jansen *et al.*, 2009; Kanduč *et al.*, 2020).

Although we do not know whether alignment of holes across different layers is required for mass flow of air across a pit membrane, misalignment of holes could reduce the likelihood of having a leaky pit membrane. There is a very low chance of having a single, large pore in a vessel with 30,000 intervessel pit membranes having a T_{PM}–value of 200 nm or more, even if extremely large holes with a diameter of 200 nm occur in a single microfibril layer (Model 2 and 3). It is possible that variation in T_{PM} within a vessel or within the vessel network provides additional chances of leakiness. Capturing this variation, however, is difficult because measuring pit membrane thickness may not be straightforward, for instance due to TEM preparation artefacts, aggregation of cellulose fibrils into larger aggregates, and seasonal shrinkage of pit membranes (Schmid & Machado, 1968; Sorek *et al.*, In press).

Aspiration or a mechanical pressure on intervessel pit membranes may explain the difference between central and marginal T_{PM}, because the marginal pit membrane area could be more compressed by deflection against the pit border than the central area that facing the aperture.

Nevertheless, this difference raises questions about the assumption that cellulose fibres are homogeneously and equally spaced from each other. It seems likely that the slightly negatively charged cellulose fibres repel each other and are more loosely arranged in the centre (Zhang *et al.*, 2016), but are more compressed near the edge, where the cellulose fibres are firmly anchored into the pectin-rich annulus and primary wall. Although the orientation of microfibrils may not be completely random and appears to be directed by a dual guidance mechanism (Chan & Coen, 2020), it seems unlikely from a developmental point of view that more cellulose fibrils are deposited in the centre than near the annulus, as could be shown for torus-bearing angiosperms (Dute, 2015)

How is the size of pore constrictions linked to embolism spreading and resistance?

Embolism spreading via pit membranes seems to depend strongly on T_{PM}, which controls the narrowest pore constriction within a pore. Pit membranes are not different from other non-woven, fibrous porous media, where the pressure required to force a gas bubble through the medium, the so-called bubble point, is a function of the thickness of the medium and its overall structure (Aydilek *et al.*, 2007). Comparison of modelled air-seeding pressures with measurements of P_{12} show strong agreement, but a clear difference in absolute values for most species (Fig. 5), with P_{12} values falling between the estimated air-seeding based on R_{MIN_mean} and R_{MIN_max} (Fig. 4a, 5b, d). Experimental data on air-seeding pressure of angiosperm xylem suggest values between 0.4 and 2 MPa (Choat *et al.*, 2004; Jansen *et al.*, 2009; Christman *et al.*, 2012; Wason *et al.*, 2018), which is more or less in line with P_{12} values of a wide range of angiosperm species (Bartlett *et al.*, 2016). Moreover, 65% of the species in our study show P_{12} values that are more negative than -2 MPa, with an average P_{12} value of -2.57 MPa, which matches the average P_{12} value of -2.65 MPa of 12 temperate angiosperm species (Schuldt *et al.*, 2020).

Embolism propagation across thin pit membranes seems to be determined by pores similar in size to R_{MIN_max} due to their large similarity between measurements of P_{12} and P_{50} with modelled air-seeding pressures based on R_{MIN_max}. In contrast, embolism spreading in species with thick pit membranes is affected by pore sizes that can be close to both R_{MIN_max} and R_{MIN_mean} (Fig. 3b, 4a). This finding is in line with the fact that high values of T_{PM_mean} show a higher standard deviation than low T_{PM_mean}, while the slope of vulnerability curves becomes lower for species with thicker pit membranes. In fact, R_{MIN_mean} is expected to provide an upper limit for air-seeding pressure,

since it is unlikely that pore constrictions smaller than R_{MIN_mean} will influence air-seeding. Accordingly, R_{MIN_max} offers the least resistance to gas moving through a pore space, and provides a good explanation for a lower limit for air-seeding pressure.

There can be various reasons why modelled air-seeding pressures do not match the absolute values of measured P_{12} values. First, the values obtained from Model 1 are based on air-seeding estimations of a single pit membrane model with a certain thicknesses, while P_{12}- and P_{50}-values represent hydraulically-weighted losses of conductivity at the the vessel network level, which is affected by various structural xylem parameters, such as vessel grouping and the ratio of T_{PM} and pit membrane area (Levionnois *et al.*, in press). Second, estimations based on the Young-Laplace equation should be interpreted with caution due to various poorly known parameters and processes. Embolism formation in a multiphase environment under negative pressure is highly complicated, for instance, by dynamic surface tension, line tension, the contact angle of the gas-liquid interface within the pit membrane, and highly variable pore sizes (Choat *et al.*, 2004; Law *et al.*, 2017; Schenk *et al.*, 2017; Satarifard *et al.*, 2018; Zhang *et al.*, 2020; Li *et al.*, 2020; Yang *et al.*, 2020). Pore constrictions and porosity could change if pit membranes become deflected and aspirated against the pit border, which could cause pit membrane shrinkage, reduced porosity and constrictivity, or rearrangement of microfibrils (Tixier *et al.*, 2014; Kotowska *et al.*, 2020; Zhang *et al.*, 2017, 2020). Yet, the mechanical properties of pit membranes remain largely unknown (Tixier *et al.*, 2014).

Moreover, it is also possible that drought-induced embolism spreading does not happen via air-seeding, i.e. mass flow of air-water menisci across intervessel pit membranes. The discovery of surfactant-coated nanobubbles in xylem sap could provide an alternative hypothesis, and highlights the importance of amphiphilic, insoluble lipids associated with pit membranes, and bubble snap-off by pore constrictions (Schenk *et al.*, 2015, 2017, 2018, 2020; Kaack *et al.*, 2019; Park *et al.*, 2019). Diffusion of gas molecules between an embolised and an adjacent vessel could represent an additional way of gas entry and embolism formation, which might be largely dependent on R_{MIN_mean} and less on R_{MIN_max} (Guan *et al.*, submitted).

Pit membrane thickness and the number of intervessel pits have different consequences on embolism resistance

We show that T_{PM} is a much stronger determinant of the likelihood of leaky pit membranes than N_{PIT} and the total intervessel pit membrane surface area (A_P). Our results do not support the rare pit hypothesis (Wheeler *et al.*, 2005; Sperry *et al.*, 2006) and provide a novel view on the relationship between N_{PIT} or A_P and embolism resistance. Most importantly, our Model 2 shows that T_{PM} and N_{PIT} affect the likelihood of encountering wide pores differently, with contrasting differences for species with a wide range of T_{PM}. The effect of N_{PIT} on vessel leakiness is limited to a narrow range of critical T_{PM}-values, depending on the assumptions made in Model 2 (Fig. 6, Fig. S4).

In a general, simplified way, three functional types of pit membranes can be distinguished based on T_{PM}: (1) a thin, risky type, with relatively large pores, a rather low embolism resistance, and little or no reduced embolism resistance for low values of N_{PIT}, (2) a thick and very safe pit membrane type, with narrow pores, high embolism resistance, and hardly any reduction of embolism resistance for high N_{PIT}, and (3) an intermediate pit membrane type, with embolism resistance strongly affected by N_{PIT}, where N_{PIT} or other xylem structural traits could potentially be modified during growth to vary embolism resistance in response to the amount of drought experienced. Unfortunately, exact T_{PM}-values to define these pit membranes types are unclear. Based on leakiness probabilities that are close to zero for $T_{PM} > 250$ nm (Models 1 and 3), and the decreasing slopes of the measured P_{50}-values with increasing T_{PM}, we roughly estimate that T_{PM} values of the intermediate type are between 150 and 300 nm. This would correspond to 60% of the species in our data set. Interestingly, the risky and safe pit membranes (types and 2) decouple hydraulic safety from hydraulic connectivity, which is suggested to increase with vessel connectivity of the xylem (Loepfe *et al.*, 2007; Schenk *et al.*, 2008; Espino & Schenk, 2009). Since hydraulic connectivity relates to efficiency, the lack of a trade-off between safety and efficiency at the pit membrane level could be suggested, which provides a novel view on the weak relationship between specific hydraulic conductivity and P_{50}-values of many angiosperm species (Hacke *et al.*, 2006; Loepfe *et al.*, 2007; Gleason *et al.*, 2016).

Overall, our results indicate that the rare pit hypothesis cannot explain embolism spreading at the whole vessel network since the functional importance of multiple pore constrictions makes it highly unlikely that many vessels contain a leaky pore for a wide range of T_{PM}. In fact, earlier studies that tested this hypothesis should be considered carefully due to possible artefacts in embolism resistance measurements (Wheeler *et al.*, 2013; Torres-Ruiz *et al.*, 2017). Also, no large

pores have ever been found in hydrated pit membranes (Schmid & Machado, 1968; Choat *et al.*, 2003, 2004; Pesacreta *et al.*, 2005; Jansen *et al.*, 2018; Zhang *et al.*, 2020). Finally, plants are unlikely to create failures in the three-dimensional development of their cell walls because the synthesis and deposition of cellulose during primary cell wall development includes highly orchestrated processes by the cytoplasm and its cytoskeleton, which reduces the likelihood of large gaps between cellulose fibrils and/or fibrillar aggregates (Chaffey *et al.*, 1997; Oda & Fukuda, 2013; Bourdon *et al.*, 2017; Sugiyama *et al.*, 2017, 2019).

Further progress in understanding embolism spreading in angiosperm xylem will strongly depend on the development of realistic three-dimensional pit membrane and vessel network models (Gaiselmann *et al.*, 2014; Li et al., 2019), combined with careful simulations of the chemical and physical interactions within a multiphase environment of gas, water, cellulose, and surfactants.

Acknowledgements

Financial support is acknowledged to SJ by a research grant from the German Research Foundation (JA 2174/5-1; nr. 383393940), to SJ and VS by the Baden-Württemberg Ministerium für Wissenschaft, Forschung und Kunst (project 7533-7-11.10-16), and to HJS and SJ by the National Science Foundation (IOS-1754850). We thank Klaus Körber from the Bavarian State Institute for Viticulture and Horticulture, Veitshochheim, Germany, for granting us access to the Stutel-Arberetum facility, as well as Andreas Lösch and all others involved in the 'Klimabäume Stutel' project. We thank various colleagues for fruitful discussions, valuable suggestions, and practical assistance in the lab.

Author contributions

LK, MW, LP, HJS, VS, SJ planned and designed the research. IE, ZK, SL, CT, YZ, BS provided experimental data. LK and MW wrote the manuscript, with input from all co-authors. LK and MW contributed equally.

References

Aydilek AH, D'Hondt D, Holtz RD. **2007**. Comparative evaluation of geotextile pore sizes using bubble point test and image analysis. *Geotechnical Testing Journal* **30**: 173–181.

Bartlett MK, Klein T, Jansen S, Choat B, Sack L. **2016**. The correlations and sequence of plant stomatal, hydraulic, and wilting responses to drought. *Proceedings of the National Academy of Sciences* **113**: 13098–13103.

Bourdon M, Kalmbach L, Helariutta Y. **2017**. Plant vasculature: selective membrane-to-microtubule tethering patterns the xylem cell wall. *Current biology: CB* **27**: R842–R844.

Brodersen CR, McElrone AJ, Choat B, Lee EF, Shackel KA, Matthews MA. **2013**. In vivo visualizations of drought-induced embolism spread in *Vitis vinifera*. *Plant Physiology* **161**: 1820–1829.

Brodribb TJ, Bienaimé D, Marmottant P. **2016**. Revealing catastrophic failure of leaf networks under stress. *Proceedings of the National Academy of Sciences* **113**: 4865–4869.

Chaffey NJ, Barnett JR, Barlow PW. **1997**. Cortical microtubule involvement in bordered pit formation in secondary xylem vessel elements of *Aesculus hippocastanum* L. (Hippocastanaceae): A correlative study using electron microscopy and indirect immunofluorescence microscopy. *Protoplasma* **197**: 64–75.

Chan J, Coen E. **2020**. Interaction between autonomous and microtubule guidance systems controls cellulose synthase trajectories. *Current Biology* **30**: 941-947.e2.

Choat B, Badel E, Burlett R, Delzon S, Cochard H, Jansen S. **2016**. Noninvasive measurement of vulnerability to drought-induced embolism by x-ray microtomography. *Plant Physiology* **170**: 273–282.

Choat B, Ball M, Luly J, Holtum J. **2003**. Pit membrane porosity and water stress-induced cavitation in four co-existing dry rainforest tree species. *Plant Physiology* **131**: 41–48.

Choat B, Cobb AR, Jansen S. **2008**. Structure and function of bordered pits: new discoveries and impacts on whole-plant hydraulic function. *New Phytologist* **177**: 608–626.

Choat B, Jansen S, Brodribb TJ, Cochard H, Delzon S, Bhaskar R, Bucci SJ, Feild TS, Gleason SM, Hacke UG, *et al.* 2012. Global convergence in the vulnerability of forests to drought. *Nature* **491**: 752–755.

Choat B, Jansen S, Zwieniecki MA, Smets E, Holbrook NM. **2004**. Changes in pit membrane porosity due to deflection and stretching: the role of vestured pits. *Journal of Experimental Botany* **55**: 1569–1575.

Christman MA, Sperry JS, Adler FR. **2009**. Testing the 'rare pit' hypothesis for xylem cavitation resistance in three species of *Acer*. *New Phytologist* **182**: 664–674.

Christman MA, Sperry JS, Smith DD. **2012**. Rare pits, large vessels and extreme vulnerability to cavitation in a ring-porous tree species. *New Phytologist* **193**: 713–720.

Dute RR. **2015**. Development, structure, and function of torus–margo pits in conifers, ginkgo and dicots. In: Hacke U, ed. Functional and Ecological Xylem Anatomy. Cham: Springer International Publishing, 77–102.

Esau K. 1977. Anatomy of seed plants (2nd ed). Wiley, NewYork.

Espino S, Schenk HJ. **2009**. Hydraulically integrated or modular? Comparing whole-plant-level hydraulic systems between two desert shrub species with different growth forms. *New Phytologist* **183**: 142–152.

Gaiselmann G, Tötzke C, Manke I, Lehnert W, Schmidt V. **2014**. 3D microstructure modeling of compressed fiber-based materials. *Journal of Power Sources* **257**: 52–64.

Gleason SM, Westoby M, Jansen S, Choat B, Hacke UG, Pratt RB, Bhaskar R, Brodribb TJ, Bucci SJ, Cao K-F, *et al.* 2016. Weak tradeoff between xylem safety and xylem-specific hydraulic efficiency across the world's woody plant species. *New Phytologist* **209**: 123–136.

Hacke UG, Sperry JS, Feild TS, Sano Y, Sikkema EH, Pittermann J. **2007**. Water transport in vesselless angiosperms: conducting efficiency and cavitation safety. *International Journal of Plant Sciences* **168**: 1113–1126.

Hacke UG, Sperry JS, Wheeler JK, Castro L. **2006**. Scaling of angiosperm xylem structure with safety and efficiency. *Tree Physiology* **26**: 689–701.

Herbette S, Bouchet B, Brunel N, Bonnin E, Cochard H, Guillon F. **2015**. Immunolabelling of intervessel pits for polysaccharides and lignin helps in understanding their hydraulic properties in *Populus tremula* × alba. *Annals of Botany* **115**: 187–199.

Hillabrand RM, Hacke UG, Lieffers VJ. **2016**. Drought-induced xylem pit membrane damage in aspen and balsam poplar. *Plant, Cell & Environment* **39**: 2210–2220.

Jansen S, Choat B, Pletsers A. **2009**. Morphological variation of intervessel pit membranes and implications to xylem function in angiosperms. *American Journal of Botany* **96**: 409–419.

Jansen S, Gortan E, Lens F, Gullo MAL, Salleo S, Scholz A, Stein A, Trifilò P, Nardini A. **2011**. Do quantitative vessel and pit characters account for ion-mediated changes in the hydraulic conductance of angiosperm xylem? *New Phytologist* **189**: 218–228.

Jansen S, Klepsch M, Li S, Kotowska M, Schiele S, Zhang Y, Schenk H. **2018**. Challenges in understanding air-seeding in angiosperm xylem. *Acta Horticulturae* **1222**: 13–20.

Jansen S, Pletsers A, Sano Y. **2008**. The effect of preparation techniques on SEM-imaging of pit membranes. *IAWA Journal* **29**: 161–178.

Kaack L, Altaner CM, Carmesin C, Diaz A, Holler M, Kranz C, Neusser G, Odstrcil M, Schenk HJ, Schmidt V, *et al.* 2019. Function and three-dimensional structure of intervessel pit membranes in angiosperms: a review. *International Association of Wood Anatomists Journal* **40**: 673–702.

Kanduč M, Schneck E, Loche P, Jansen S, Schenk HJ, Netz RR. **2020**. Cavitation in lipid bilayers poses strict negative pressure stability limit in biological liquids. *Proceedings of the National Academy of Sciences of the United States of America* **117**: 10733–10739.

Karimi Z, 2014. Systematic, Evolutionary and Functional Anatomy of Wood and Leaves in Betulaceae. PhD thesis, Ulm University, BW, Germany.

Klepsch MM, Schmitt M, Paul JK, Jansen S. **2016**. The chemical identity of intervessel pit membranes in *Acer* challenges hydrogel control of xylem hydraulic conductivity. *Annals of Botany PLANTS* **8**.

Kotowska MM, Thom R, Zhang Y, Schenk HJ, Jansen S. **2020**. Within-tree variability and sample storage effects of bordered pit membranes in xylem of *Acer pseudoplatanus*. *Trees* **34**: 61–71.

Law BM, McBride SP, Wang JY, Wi HS, Paneru G, Betelu S, Ushijima B, Takata Y, Flanders B, Bresme F, *et al.* 2017. Line tension and its influence on droplets and particles at surfaces. *Progress in Surface Science* **92**: 1–39.

Lens F, Sperry JS, Christman MA, Choat B, Rabaey D, Jansen S. **2011**. Testing hypotheses that link wood anatomy to cavitation resistance and hydraulic conductivity in the genus *Acer*. *The New Phytologist* **190**: 709–723.

Levionnois S, Jansen S, Wandji RT, Beauchêne J, Ziegler C, Coste S, Stahl C, Delzon S, Authier L, Heuret P. (2020) Linking drought-induced xylem embolism resistance to wood anatomical traits in Neotropical trees. *New Phytologist* doi.org/10.1111/nph.16942.

Li S, Lens F, Espino S, Karimi Z, Klepsch M, Schenk HJ, Schmitt M, Schuldt B, Jansen S. **2016**. Intervessel pit membrane thickness as a key determinants of embolism resistance in angiosperm xylem. *IAWA Journal* **37**: 152–171.

Li S, Wang J, Yin Y, Li X, Deng L, Jiang X, Chen Z, Li Y. **2020**. Investigating effects of bordered pit membrane morphology and properties on plant xylem hydraulic functions — A case study from 3D reconstruction and microflow modelling of pit membranes in angiosperm xylem. *Plants* **9**: 231.

Loepfe L, Martinez-Vilalta J, Piñol J, Mencuccini M. **2007**. The relevance of xylem network structure for plant hydraulic efficiency and safety. *Journal of Theoretical Biology* **247**: 788–803.

Mrad A, Domec J-C, Huang C-W, Lens F, Katul G. **2018**. A network model links wood anatomy to xylem tissue hydraulic behaviour and vulnerability to cavitation. *Plant, Cell & Environment* **41**: 2718–2730.

Nardini A, Dimasi F, Klepsch M, Jansen S. **2012**. Ion-mediated enhancement of xylem hydraulic conductivity in four *Acer* species: relationships with ecological and anatomical features. *Tree Physiology* **32**: 1434–1441.

O'Brien TP. **1970**. Further observations on hydrolysis of the cell wall in the xylem. *Protoplasma* **69**: 1–14.

Oda Y, Fukuda H. **2013**. Rho of plant GTPase signaling regulates the behavior of Arabidopsis Kinesin-13A to establish secondary cell wall patterns. *The Plant Cell* **25**: 4439–4450.

Park J, Go T, Ryu J, Lee SJ. **2019**. Air spreading through wetted cellulose membranes: Implications for the safety function of hydraulic valves in plants. *Physical Review E* **100**: 032409.

Pesacreta TC, Groom LH, Rials TG. **2005**. Atomic force microscopy of the intervessel pit membrane in the stem of *Sapium sebiferum* (Euphorbiaceae). *IAWA Journal* **26**: 397–426.

Plavcová L, Hacke UG. **2012**. Phenotypic and developmental plasticity of xylem in hybrid poplar saplings subjected to experimental drought, nitrogen fertilization, and shading. *Journal of Experimental Botany* **63**: 6481–6491.

Plavcová L, Jansen S, Klepsch M, Hacke UG. **2013**. Nobody's perfect: can irregularities in pit structure influence vulnerability to cavitation? *Frontiers in Plant Science* **4**: 453.

Roth-Nebelsick A. **2019**. It's contagious: calculation and analysis of xylem vulnerability to embolism by a mechanistic approach based on epidemic modeling. *Trees*.

Sano Y. **2005**. Inter- and intraspecific structural variations among intervascular pit membranes, as revealed by field-emission scanning electron microscopy. *American Journal of Botany* **92**: 1077–1084.

Satarifard V, Grafmüller A, Lipowsky R. **2018**. Nanodroplets at membranes create tight-lipped membrane necks via negative line tension. *ACS Nano* **12**: 12424–12435.

Schenk HJ, Espino S, Goedhart CM, Nordenstahl M, Cabrera HIM, Jones CS. **2008**. Hydraulic integration and shrub growth form linked across continental aridity gradients. *Proceedings of the National Academy of Sciences* **105**: 11248–11253.

Schenk HJ, Espino S, Romo DM, Nima N, Do AYT, Michaud JM, Papahadjopoulos-Sternberg B, Yang J, Zuo YY, Steppe K, *et al.* 2017. Xylem surfactants introduce a new element to the cohesion-tension theory. *Plant Physiology* **173**: 1177–1196.

Schenk HJ, Michaud JM, Mocko K, Espino S, Melendres T, Roth MR, Welti R, Kaack L, Jansen S. 2020. Lipids in xylem sap of woody plants across the angiosperm phylogeny. bioRxiv:763771. https://doi.org/10.1101/763771.

Schmid R, Machado RD. **1968**. Pit membranes in hardwoods—Fine structure and development. *Protoplasma* **66**: 185–204.

Scholz A, Rabaey D, Stein A, Cochard H, Smets E, Jansen S. **2013**. The evolution and function of vessel and pit characters with respect to cavitation resistance across 10 *Prunus* species. *Tree Physiology* **33**: 684–694.

Schuldt B, Buras A, Arend M, Vitasse Y, Beierkuhnlein C, Damm A, Gharun M, Grams TEE, Hauck M, Hajek P, *et al.* 2020. A first assessment of the impact of the extreme 2018 summer drought on Central European forests. *Basic and Applied Ecology* **45**: 86–103.

Schuldt B, Knutzen F, Delzon S, Jansen S, Müller-Haubold H, Burlett R, Clough Y, Leuschner C. 2016. How adaptable is the hydraulic system of European beech in the face of climate change-related precipitation reduction? *New Phytologist* **210**: 443–458.

Shane MW, McCully ME, Canny MJ. 2000. Architecture of branch-root junctions in maize: structure of the connecting xylem and the porosity of pit membranes. *Annals of Botany* **85**: 613–624.

Sorek Y, Grinshtein S, Netzer Y, Shtein I, Jansen S, Hochberg U. 2020. An increase in xylem embolism resistance of grapevine leaves during the growing season is coordinated with stomatal regulation, turgor loss point, and intervessel pit membranes. *New Phytologist*, in press.

Sperry JS, Hacke UG. 2004. Analysis of circular bordered pit function I. Angiosperm vessels with homogenous pit membranes. *American Journal of Botany* **91**: 369–385.

Sperry JS, Hacke UG, Pittermann J. 2006. Size and function in conifer tracheids and angiosperm vessels. *American Journal of Botany* **93**: 1490–1500.

Sugiyama Y, Nagashima Y, Wakazaki M, Sato M, Toyooka K, Fukuda H, Oda Y. 2019. A Rho-actin signaling pathway shapes cell wall boundaries in Arabidopsis xylem vessels. *Nature Communications* **10**: 468.

Sugiyama Y, Wakazaki M, Toyooka K, Fukuda H, Oda Y. 2017. A novel plasma membrane-anchored protein regulates xylem cell-wall deposition through microtubule-dependent lateral inhibition of Rho GTPase domains. *Current Biology* **27**: 2522-2528.e4.

Tixier A, Herbette S, Jansen S, Capron M, Tordjeman P, Cochard H, Badel E. 2014. Modelling the mechanical behaviour of pit membranes in bordered pits with respect to cavitation resistance in angiosperms. *Annals of Botany* **114**: 325–334.

Torres-Ruiz JM, Cochard H, Choat B, Jansen S, López R, Tomášková I, Padilla-Díaz CM, Badel E, Burlett R, King A, *et al.* 2017. Xylem resistance to embolism: presenting a simple diagnostic test for the open vessel artefact. *New Phytologist* **215**: 489–499.

Vilagrosa A, Cortina J, Gil-Pelegrín E, Bellot J. 2003. Suitability of drought-preconditioning techniques in mediterranean climate. *Restoration Ecology* **11**: 208–216.

Wason JW, Anstreicher KS, Stephansky N, Huggett BA, Brodersen CR. 2018. Hydraulic safety margins and air-seeding thresholds in roots, trunks, branches and petioles of four northern hardwood trees. *New Phytologist* **219**: 77–88.

Wheeler JK, Huggett BA, Tofte AN, Rockwell FE, Holbrook NM. 2013. Cutting xylem under tension or supersaturated with gas can generate PLC and the appearance of rapid recovery from embolism. *Plant, Cell & Environment* **36**: 1938–1949.

Wheeler JK, Sperry JS, Hacke UG, Hoang N. **2005**. Inter-vessel pitting and cavitation in woody Rosaceae and other vesselled plants: a basis for a safety versus efficiency trade-off in xylem transport. *Plant, Cell & Environment* **28**: 800–812.

Guan X, Pereira L, McAdam S, Cao KF, Jansen S. 2020. No gas source, no problem: pre-existing embolism may affect non-pressure driven embolism spreading in angiosperm xylem by gas diffusion. DOI: 10.22541/au.159674582.24283294, submitted.

Yang J, M Michaud J, Jansen S, Schenk HJ, Zuo YY. **2020**. Dynamic surface tension of xylem sap lipids. *Tree Physiology* 40: 433–444.

Zhang Y, Carmesin C, Kaack L, Klepsch MM, Kotowska M, Matei T, Schenk HJ, Weber M, Walther P, Schmidt V, *et al.* 2020. High porosity with tiny pore constrictions and unbending pathways characterize the 3D structure of intervessel pit membranes in angiosperm xylem. *Plant, Cell & Environment* **43**: 116–130.

Zhang Y, Klepsch M, Jansen S. **2017**. Bordered pits in xylem of vesselless angiosperms and their possible misinterpretation as perforation plates. *Plant, Cell & Environment* **40**: 2133–2146.

Zhang H, Zhao C, Li Z, Li J. **2016**. The fiber charge measurement depending on the poly-DADMAC accessibility to cellulose fibers. *Cellulose* **23**: 163–173.

Zimmermann MH. **1983**. *Xylem Structure and the Ascent of Sap*. New York: Springer-Verlag.

Table 1. Overview of pit membrane thickness values (T_{PM}, nm) and their corresponding numbers of microfibril layers (N_L) according to the shrinkage model of Zhang et al. (2019). Assuming a homogeneous distribution of cellulose fibres, which have a diameter of 20 nm and a distance of 20 nm from each other, $N_L = (T_{PM} + 20) / 40$.

T_{PM} [nm]	140	300	460	620	780	940	1100	1260
N_L	4	8	12	16	20	24	28	32

723 **Table 2:** Overview of the abbreviations of modelling and experimental parameters used with
724 reference to their units and definitions.

Modelling acronym	**Units**	**Definition**
n		Sample size
P	/	Probability of encountering at least one hole larger than a given threshold in any given layer of a pit membrane.
Nc	/	Number of constrictions in a pore, which equals N_L
N_{HOLES}	/	Number of large, non-overlapping holes with random positions in a single pit membrane layer
N_L	/	Number of microfibril layers in a pit membrane; $N_L = (T_{PM} + 20) / 40$
N_P	/	Total number of pores in an intervessel pit membrane
N_{PIT}	/	Average number of intervessel pits for a vessel with average length and diameter
μ_R, σ_R, R_L	nm	Parameters of the left-truncated normal distribution modelling pore constriction radii in Model 1
P_{LP}	/	Probability of a leaky pit membrane occurring in an average vessel
R_{MIN}	nm	Radius of the narrowest constriction in a pore
R_{MIN_max}	nm	Maximum R_{MIN} value of all pores in a single pit membrane
R_{MIN_mean}	nm	Mean R_{MIN} value of all pores in a single pit membrane
t	/	Minimal size of a pore, a pore constriction, or a hole to be considered as 'large'
Experimental acronym	**Units**	**Definition**

A_P	mm^2	Total intervessel pit membrane surface area for a vessel with average length and diameter
P_{12}, P_{50}, P_{88}	MPa	Xylem water potential corresponding to 12%, 50% and 88% loss of maximum hydraulic conductivity, respectively
S	%/MPa	Slope of a vulnerability curve
T_{PM_mean}, T_{PM_centre}, T_{PM_edge}	nm	Intervessel pit membrane thickness as measured on TEM images of freshly embedded xylem samples; mean value, value around the centre, and near the edges of a pit membrane (excluding pit membrane annuli)

725

726

Table 3. Overview of the r- and R^2-values between pit anatomical characteristics and embolism resistance. Anatomical measurements include mean values of the intervessel pit membrane thickness (T_{PM_mean}), central measurements (T_{PM_centre}), those near the pit membrane annulus (T_{PM_edge}), and the total intervessel pit membrane area per vessel (A_P). Embolism resistance has been quantified as xylem water potential values corresponding to 12% (P_{12}), 50% (P_{50}), and 88% (P_{88}) loss of the maximum hydraulic conductivity based on vulnerability curves. The estimation of air seeding pressure is either based on the largest value of R_{MIN} across all pores of a membrane (Air seeding R_{MIN_max}) or the mean value of R_{MIN} across all pores of a membrane (Air seeding R_{MIN_mean}), using a modified Young-Laplace equation. The regression models that show the strongest relation are given here. Logarithmic regression[1]; power regression[2]; Pearson Coefficient Correlation[3]; p-values: < 0.05 = *, < 0.01 = **, < 0.001***.

	P_{12}	P_{50}	P_{88}	S	T_{PM_mean} SD
T_{PM_centre}	0.457 ***[1]	0.571 ***[1]	0.541 ***[1]	0.485 ***[2]	NA
T_{PM_mean}	0.439 ***[1]	0.556 ***[1]	0.525 ***[1]	0.477 ***[2]	0.759 ***[3]
T_{PM_edge}	0.306 **[1]	0.410 ***[1]	0.392 ***[1]	0.340 ***[2]	NA
A_P	0.301 *[1]	0.252 *[1]	0.221 *[1]	0.103 ***[2]	NA
Air seeding R_{MIN_max}	0.636 ***[3]	0.732 ***[3]	NA	NA	NA
Air seeding R_{MIN_mean}	0.670 ***[3]	0.739 ***[3]	NA	NA	NA

739 **Figures**

740

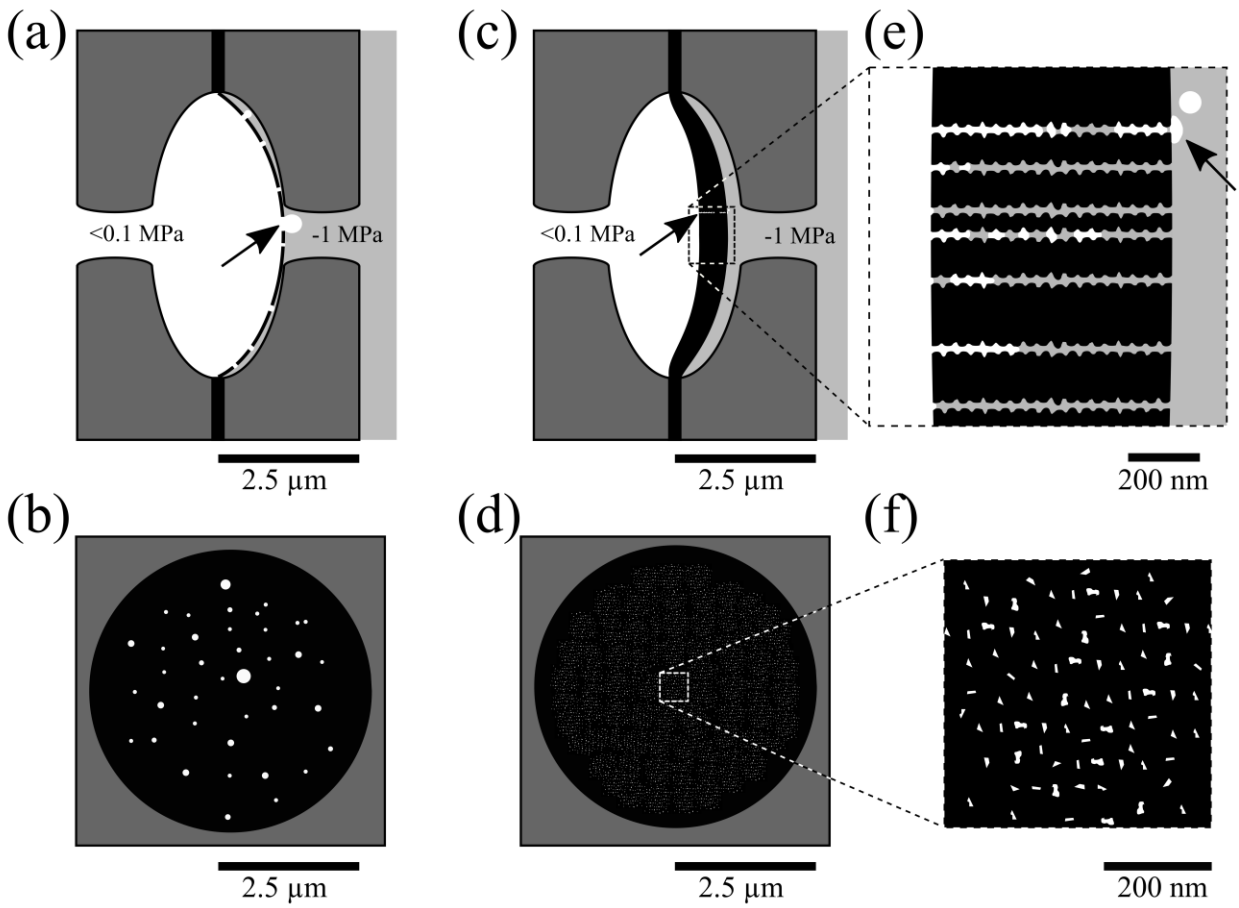

741 **Figure 1**. Drawings illustrating a mainly two-dimensional (a, b) and three-dimensional (c, d, e, f)
742 concept of angiosperm pit membranes and air-seeding under aspiration. The upper images (a, c, e)
743 show a longitudinal view, while the bottom ones (b, d, f) represent frontal views. Large, cylindrical
744 pores with circular cross-sections occur in a pit membrane, with no defined thickness, and the
745 largest pore triggers air-seeding (arrows in a, c, e). Pores in a 670 nm thick pit membrane that is
746 composed of multiple layers of cellulose fibrillar aggregates show multiple pore constrictions,
747 which greatly reduces the size of the narrowest constriction within a pore (c, f). A magnified view
748 is shown in e and f, with seven pores in e), 18 pore constrictions per idealised pore cylinder. White
749 colour = gas; bright grey = xylem sap; black = solid phase of the primary cell wall, middle lamella
750 or pit membrane, dark grey = secondary cell wall.

751

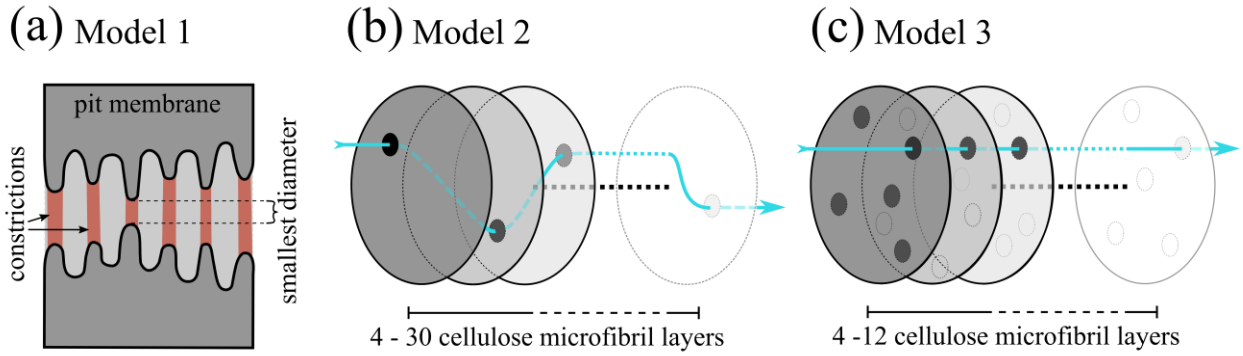

Figure 2. Three mathematical models to investigate the functional link between pit membrane thickness and effective diameters of pores. Model 1 (a) is based on a random number model to estimate the size of the narrowest constrictions of pores that traverse an entire pit membrane. This model was run ten times on a Scenario 1 with smaller and a Scenario 2 with larger pore constrictions for 12,000 or 1,100 pores per pit membrane, respectively, with 4 to 30 constrictions per pore in 140 to 1,200 nm thick pit membranes. Model 2 (b) examines the probability of large pores in 3,000 to 400,000 intervessel pit membranes within an entire vessel. Pit membranes included from four to 30 microfibril layers, assuming either a 25% or 50% chance of encountering a large hole in each layer. This model is independent of what we consider a large pore, and does not incorporate alignment of pore constrictions. Model 3 (c) evaluates the probability of encountering pores with a large effective radius at the vessel level (i.e. for 30,000 intervessel pits), with pit membranes consisting of 4 to 12 microfibril layers, assuming 5 or 10 pore constrictions of 200 nm per layer. Alignment of pore constrictions was included in Model 3 by simulating random locations of pore constrictions in each pit microfibril, and requiring minimal overlap between consecutive pore connections to create a pore. Different shades of grey represent various microfibril layers, and a hypothetical flow path is indicated by the blue lines in (b) and (c).

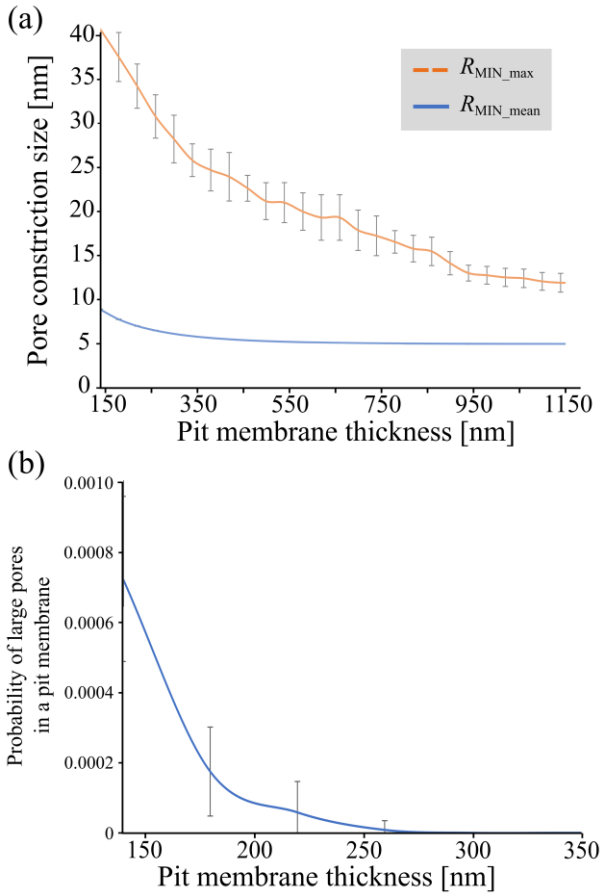

Figure 3. Results of Scenario 1 of Model 1, showing the pit membrane thickness plotted versus the pore constriction diameter based on Model 1 (a), and the likelihood of a relatively large R_{MIN_max} (≥ 35 nm) within a pit membrane (b), which decreased exponentially from 0.0008 ± 0.0002 to values approaching zero with increasing pit membrane thickness. A random number model was used, with the mean pore constriction size set to 20 ± 15 nm, and a minimum size of 5 nm. Pore constriction sizes were determined ten times for 12,000 simulated pores, corresponding to an average sized pit membrane.

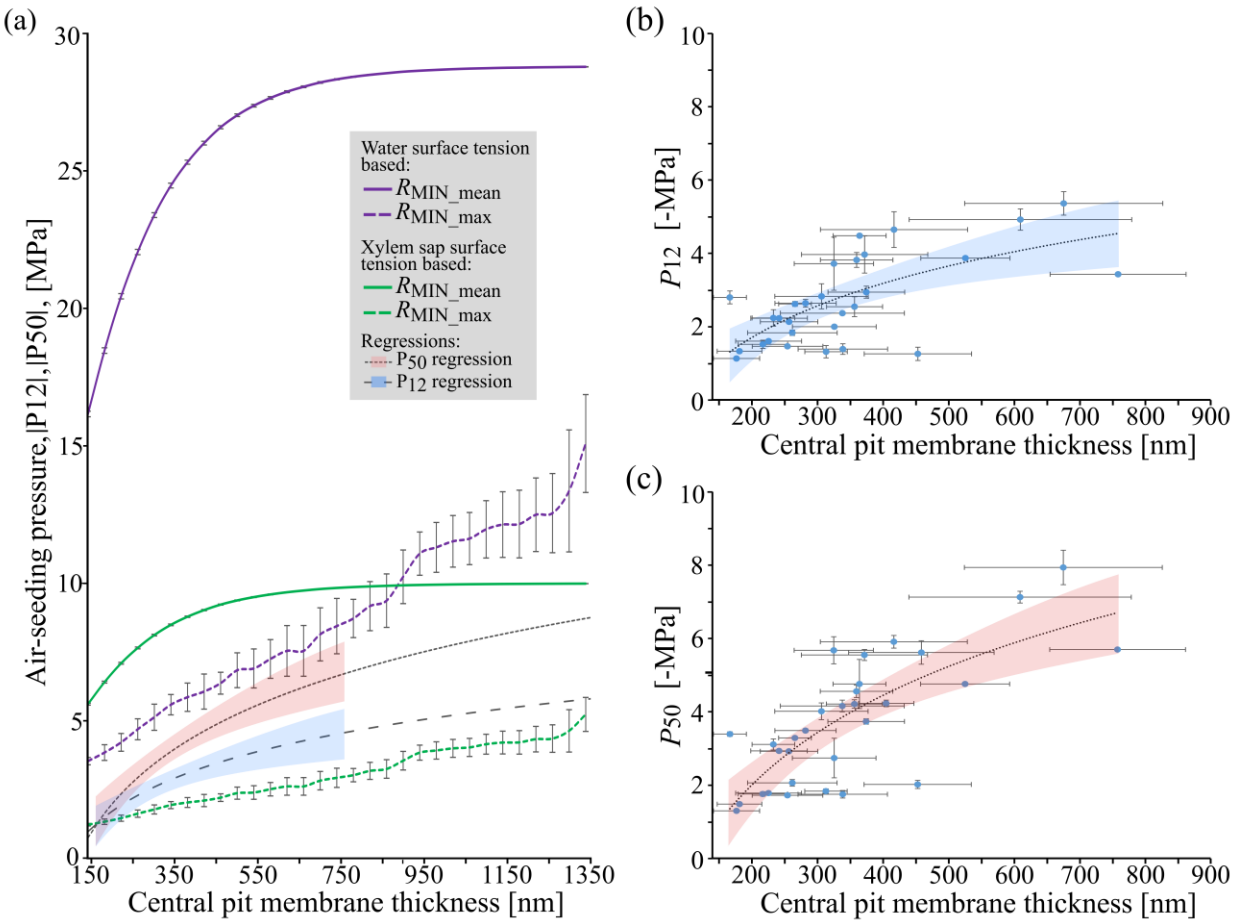

779 **Figure 4**. The relationship between pit membrane thickness and the modelled air-seeding pressure
780 (a), measured P_{12} values (b), and measured P_{50} values of 31 angiosperm angiosperms (c). Modelled
781 air-seeding pressures were based on the largest value of R_{MIN_max} (a; dotted green and purple lines),
782 and R_{MIN_min} across all pores of a membrane (a; solid green and purple lines) for pit membranes
783 with a wide range of thicknesses according to Model 1. We applied a modified Young-Laplace
784 equation to obtain air-seeding pressure values for both 72 mN/m (purple lines) and 25 mN/m
785 (green lines) surface tension (a). P_{12} and P_{50} values based on a flow-centrifuge method and
786 microCT measurements plotted against central pit membrane thickness (T_{PM}) measurements. T_{PM}
787 was based on TEM of 31 plant species. Logarithmic regression line in dark grey (dashed) and
788 corresponding confidence intervals (P_{12} = blue, P_{50} = red). In a) theses regression lines and
789 confidence intervals are incorporated (P_{12} regression = wider dotted dark grey line, blue; P_{50}
790 regression = denser dotted dark grey line, red).

791

792

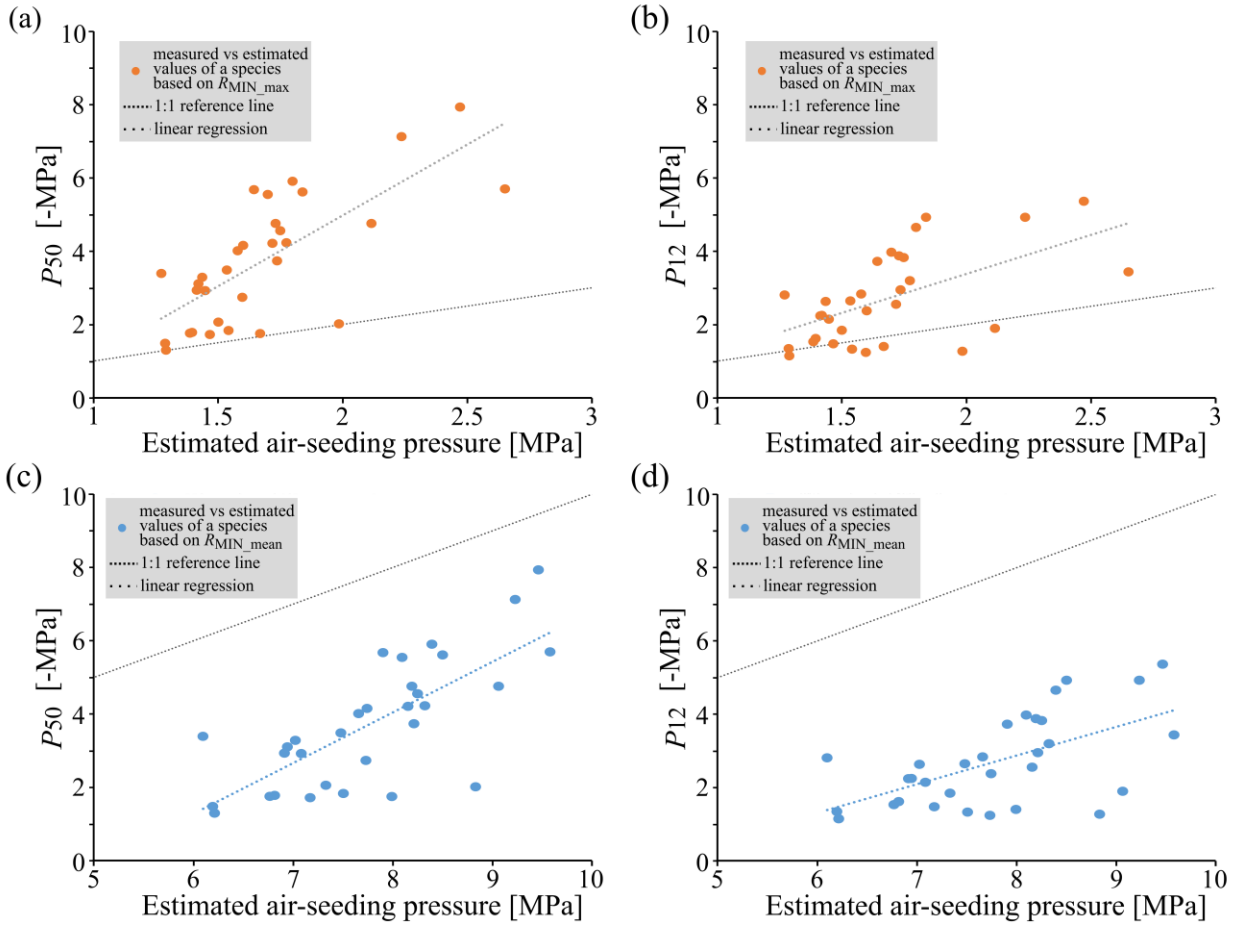

793 **Figure 5.** Modelled air-seeding pressure based on R_{MIN_max} (a, b) and R_{MIN_mean} (c, d) following

794 Scenario 1 of Model 1 versus measured P_{50} (a, c) and P_{12} (b, d) for 31 angiosperm species.

795

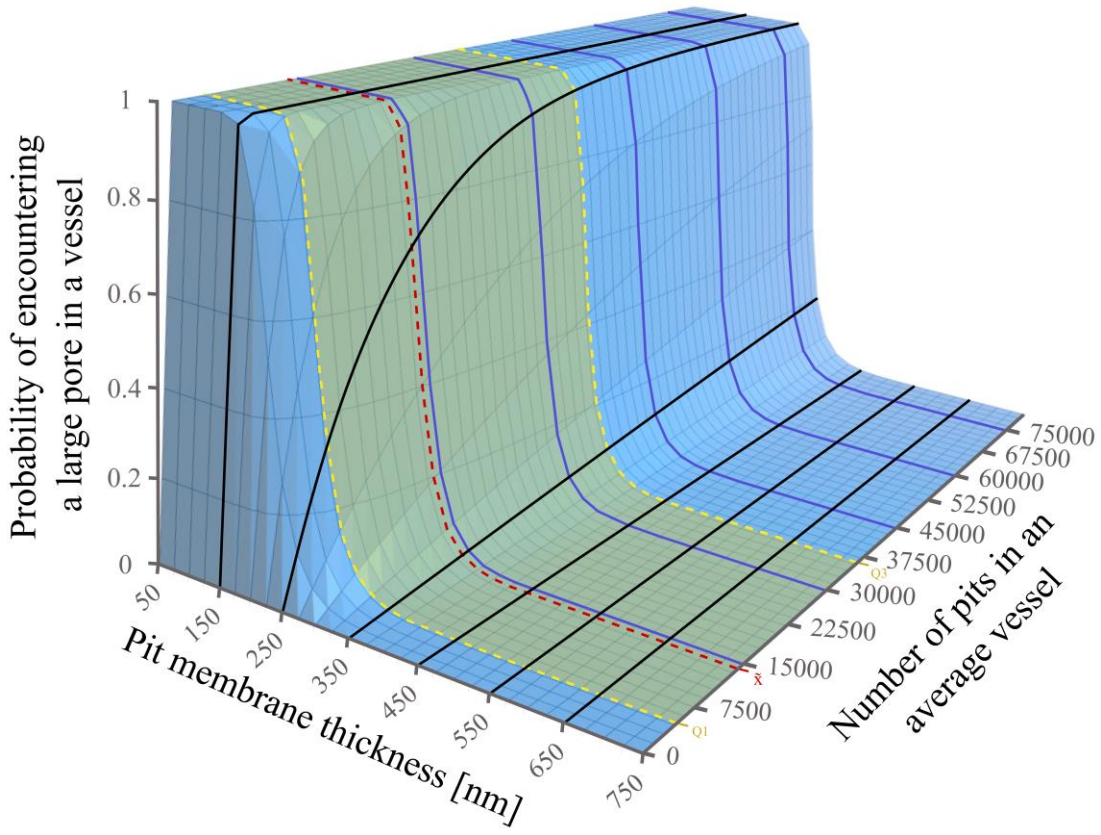

796 **Figure 6.** The probability of encountering at least one pore with large effective diameters in
797 intervessel pit membranes for an entire vessel decreases with increasing pit membrane thickness
798 (blue lines), but increases with increasing number of pits (black lines) according to Model 2. The
799 likelihood of having a large hole within a single microfibril layer was assumed to be ≤ 0.25. This
800 model did not consider the actual size of the pore constriction and ignored whether or not a hole
801 was aligned with other holes in adjacent membrane layers. The green area indicates where most
802 angiosperm species occur based on the number of intervessel pits per vessel, with the median (red
803 dotted line), and the first and third quartile (yellow dotted line).

804

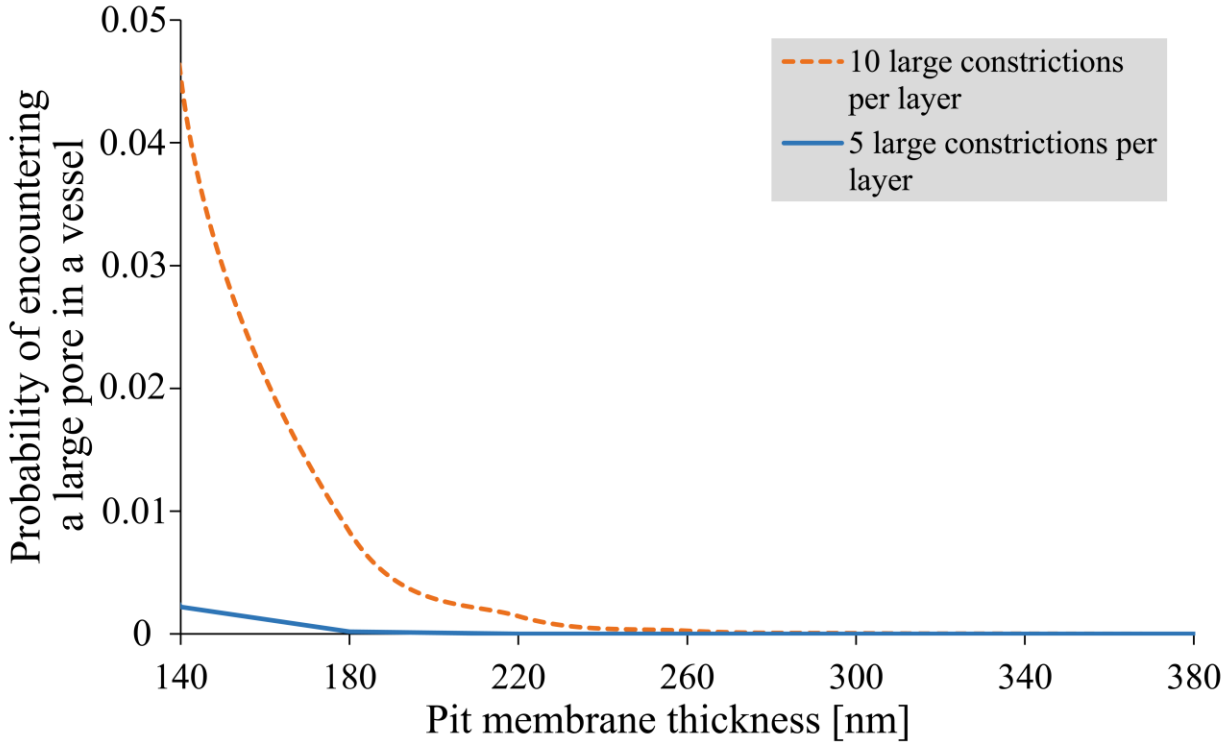

Figure 7. Output of Model 3, which assumed that intervessel pit membranes have a diameter of 5 µm, thicknesses between 140 nm and 460 nm, and an estimated number of 30,000 pits per vessel. Minimal overlapping of holes was required to obtain a pore through the whole membrane. The probability of pores with effective radius larger than a given threshold decreased exponentially in pit membranes of 140 nm to 260 nm in thickness when 10 holes of 200 nm in diameter occurred per pit membrane layer (orange line). Assuming 5 pore constrictions per layer (blue line) showed a very low likelihood of large pores, even for 140 nm thick pit membranes.

Supporting Information

Additional supporting information may be found in the online version of this article.

Fig. S1 Frequency distribution of the number of intervessel pits per average vessel.

Fig. S2 TEM images of intervessel pit membranes of different thickness.

Fig. S3 Results of Model 1, Scenario 2; relation of TPM and pore constriction size.

Fig. S4 Three-dimensional graph based on the risky scenario of Model 2, with 0.5 probability of having a large pore in a single pit membrane layer.

Fig. S5 Two-dimensional graph based on Model 2 showing the probability of a large pore in a vessel of up 400,000 pits per vessl.

Table S1 Dataset of the 31 angiosperm species studied, with reference to the anatomical and hydraulic traits measured.

Methods S1 R script of Model 3

Methods S2 Protocols: plant material, xylem embolism resistance, transmission electron microscopy, vessel and pit dimension